Biophysical Journal Volume 108 May 2015 2126–2136

Article

# Viscoelastic Transient of Confined Red Blood Cells

Gaël Prado,[1,2] Alexander Farutin,[1,2,3] Chaouqi Misbah,[1,2] and Lionel Bureau[1,2,*]

[1]Laboratoire Interdisciplinaire de Physique, Centre National de la Recherche Scientifique, Grenoble, France; [2]Laboratoire Interdisciplinaire de Physique, University Grenoble Alpes, Grenoble, France; and [3]Experimental Physics, Saarland University, Saarbrücken, Germany

ABSTRACT The unique ability of a red blood cell to flow through extremely small microcapillaries depends on the viscoelastic properties of its membrane. Here, we study in vitro the response time upon flow startup exhibited by red blood cells confined into microchannels. We show that the characteristic transient time depends on the imposed flow strength, and that such a dependence gives access to both the effective viscosity and the elastic modulus controlling the temporal response of red cells. A simple theoretical analysis of our experimental data, validated by numerical simulations, further allows us to compute an estimate for the two-dimensional membrane viscosity of red blood cells, $\eta_{\mathrm{mem}}^{2\mathrm{D}} \sim 10^{-7}$ N•s•m$^{-1}$. By comparing our results with those from previous studies, we discuss and clarify the origin of the discrepancies found in the literature regarding the determination of $\eta_{\mathrm{mem}}^{2\mathrm{D}}$, and reconcile seemingly conflicting conclusions from previous works.

## INTRODUCTION

The study of blood flow properties is a highly active field of research, both experimentally (1) and theoretically (2–4). Identifying the relevant (bio)physical parameters controlling such properties is of great interest in the context of diagnosis of blood disorders, and also represents an important fundamental challenge in numerical and theoretical modeling of complex fluids. Blood is a suspension of cellular elements (red and white blood cells, platelets) in a carrier fluid (plasma). It is known to behave as a non-Newtonian fluid, the complex rheology of which is mainly due to the presence of red blood cells (RBC), its major cellular component (1). The flow properties of blood are thus essentially governed by the concentration of RBCs (the so-called hematocrit), their mutual interactions, and their individual mechanical properties. Over the past 50 years, the latter have been the focus of numerous studies aiming at characterizing or modeling the viscoelastic behavior of individual RBCs, and in particular that of the cell membrane, which separates the outer suspending plasma from the inner cytoplasm (5–12). The membrane region comprises a lipid bilayer, an external glycocalyx layer, and an inner two-dimensional cytoskeleton composed of a spectrin network. The inner and outer layers are connected to the bilayer through transmembrane proteins. Mechanical properties of the membrane are typically described in terms of bending and expansion moduli of the bilayer, a two-dimensional elastic shear modulus of the spectrin network ($\mu_s$), and a two-dimensional membrane viscosity ($\eta_{\mathrm{mem}}^{2\mathrm{D}}$) (6,7).

Aside from their influence on bulk rheology, the membrane properties of RBCs are also of utmost importance in microconfined flows, i.e., in the microvascular network, where they control the ability of cells to adapt their shape and flow through channels having dimensions on the order of or smaller than the size of unstrained RBCs. Such a capacity of RBCs to flow through very small channels is central in their physiological function of oxygen delivery to tissue, and alterations of the viscoelasticity of RBCs are recognized to be associated with various pathologies (13). In this context, as of this writing, in vitro studies of microconfined flows are viewed as a potential diagnosis tool to discriminate between healthy and pathological cells (14–16).

Along this line, several works have investigated the steady-state behavior of confined RBCs, from the theoretical (17,18), numerical (19–21), and experimental (16,22–25) points of view, to probe, e.g., the influence of mechanical properties on cell shape or velocity. On the other hand, a limited number of studies have investigated the behavior of RBCs in transient situations. Early studies have investigated the relaxation of RBC deformation after the removal of an applied mechanical stress: the pioneer work by Hochmuth et al. (26) focused on shape recovery in micropipette experiments; Baskurt and Meiselman (27) later performed rheooptical strain relaxation experiments upon cessation of shear of concentrated RBC suspension, and Bronkhorst et al. (28) pioneered the use of optical tweezers to conduct shape-recovery experiments on single cells. More recently, Tomaiuolo and Guido (15) have performed measurements of RBC response time upon flow start in microchannels, and Braunmüller et al. (29) have investigated RBC shape relaxation using microfluidic tools.

The above studies have provided consistent results for the timescale controlling shape relaxation (or establishment) of

*Submitted September 19, 2014, and accepted for publication March 24, 2015.*

*Correspondence: lionel.bureau@ujf-grenoble.fr

Editor: Tobias Baumgart.



0006-3495/15/05/2126/11 $2.00

http://dx.doi.org/10.1016/j.bpj.2015.03.046

healthy RBCs: $\tau_c \simeq 0.1$–$0.2$ s. Moreover, chemical or physical treatments known to affect the mechanical properties of RBCs were observed to clearly modify this characteristic time (15,27). From such measurements, authors concluded that $\tau_c$ was indeed governed by the viscoelastic properties of RBCs. Following Evans and Hochmuth (30), $\tau_c$ has been commonly related to the mechanical properties of the cell as: $\tau_c = \eta_{\mathrm{mem}}^{2\mathrm{D}}/\mu_s$. Using typical values $\mu_s$ ~5–10 $\mu\mathrm{N\cdot m^{-1}}$ taken from the literature (15,26), a two-dimensional membrane viscosity $\eta_{\mathrm{mem}}^{2\mathrm{D}}$ ~$0.5$–$1 \times 10^{-6}$ $\mathrm{N\cdot s\cdot m^{-1}}$ has been computed from the measured $\tau_c$ (15,16,26,27). Puzzlingly, such studies of the transient response of RBCs conclude to a value of the membrane viscosity that contrasts with that coming from other groups of experiments, which instead yield $\eta_{\mathrm{mem}}^{2\mathrm{D}} \lesssim 10^{-7}$ $\mathrm{N\cdot s\cdot m^{-1}}$ (31–33).

The origin of such a discrepancy between the few experimental determinations of the membrane viscosity is a long-standing issue and is still an open question. However, the membrane viscosity is often a required input parameter, either for experimental data analysis (34) or in advanced numerical models of RBCs (2,11,35). In the perspective of, e.g., quantitative numerical studies of the flow behavior of suspensions of RBCs, there is therefore a clear need for a more detailed knowledge of the membrane viscosity.

We address this question in this article. We present an analytical model that describes the shape evolution of a RBC in shear flow, which we validate using three-dimensional numerical simulations. We use this framework to analyze the results of startup flow experiments. The latter are performed in the spirit of the study by Tomaiuolo and Guido (15): we extend the work of these authors, and probe the effect on $\tau_c$ of 1) the flow strength, 2) the viscosity of the suspending fluid ($\eta_{\mathrm{out}}$), and 3) a chemical treatment known to affect the intrinsic mechanical properties of RBCs.

We find that $\tau_c$ depends on the flow strength, and exploit this dependence to extract, in an original way, both the effective viscosity and the elastic modulus governing the characteristic transient time of RBCs. We then demonstrate that such an effective viscosity is not identical to the membrane viscosity, but can be used to determine the actual $\eta_{\mathrm{mem}}^{2\mathrm{D}}$. Doing so, we obtain a value of $\eta_{\mathrm{mem}}^{2\mathrm{D}}$, which is in good agreement with the low values reported by Tran-Son-Tay et al. (32). By combining theoretical, numerical, and experimental efforts in this study of viscoelastic transients of RBCs, we are thus able to reconcile the seemingly conflicting results regarding membrane viscosity of RBCs.

## Theoretical framework

### *Qualitative discussion*

The membrane of a RBC as well as the internal and external fluids are characterized by their respective viscosities

$$\eta_{\mathrm{mem}}, \eta_{\mathrm{in}}, \text{ and } \eta_{\mathrm{out}}, \text{ with } \eta_{\mathrm{mem}} = \eta_{\mathrm{mem}}^{2\mathrm{D}}/R,$$

where $R$ designates the radius of a sphere having the same surface area as that of a RBC. RBC deformation due to external flow is accompanied by dissipation in the three fluids. Because one expects the slow mechanism to govern dynamics, this entails that the three regions act as dashpots in parallel, so that the total effective dissipation coefficient can be written as

$$\eta_{\mathrm{eff}} = \alpha\eta_{\mathrm{out}} + \beta'\eta_{\mathrm{in}} + \gamma'\eta_{\mathrm{mem}},$$

where $\alpha$, $\beta'$, and $\gamma'$ are dimensionless numbers (to be specified below). A RBC under external flow experiences viscous stresses on the order of $\eta_{\mathrm{out}}V/R$. These stresses are balanced by the elastic stresses in the cell and by the viscous stresses due to cell deformation. The elastic stresses in the cell can be decomposed into two contributions: bending and shear elasticity on the one hand, and membrane inextensibility on the other. Calling respectively $\kappa$ and $\mu_s$ the bending and shear moduli of the RBC (with $\kappa$ having the dimension of an energy and $\mu_s$ the dimension of a force per unit length), the first contribution is on the order of

$$\left(\kappa/R^3 + \mu_s/R\right)f = K_{\mathrm{eff}}f/R,$$

where $f$ is the dimensionless amplitude of membrane deformation. The stress due to membrane tension reads $\zeta f/R$, where the characteristic membrane tension $\zeta$ has the dimension of a force per unit length. Membrane tension builds up in response to the forces created by the applied external flow, hence $\zeta \simeq \eta_{\mathrm{out}}V$ (this is confirmed by numerical simulations, as shown below). The viscous stress that accompanies the deformation of a RBC is ~ $\eta_{\mathrm{eff}}\dot{f}$. Balancing the stresses, we obtain the following equation for cell deformation $f$ (more details regarding the derivation of the various terms entering this stress balance can be found in the Supporting Material):

$$\eta_{\mathrm{out}}V/R = \eta_{\mathrm{eff}}\dot{f} + \left(K_{\mathrm{eff}}/R + \zeta/R\right)f. \qquad (1)$$

Note that the same form of shape evolution equations has been obtained by a rigorous derivation for almost spherical vesicles (36–40). Analyzing Eq. 1, we get that the stationary deformation $f_0$ (corresponding to $\dot{f} = 0$) reaches saturation for flow rate tending to infinity (because $\zeta \propto V$). This is a consequence of the membrane inextensibility. Rewriting Eq. 1 with $f = \delta f + f_0$, we obtain for $\delta f$ the same Eq. 1 but now with the left-hand side equal to 0. From this equation, we can calculate the inverse relaxation time $\tau_c^{-1}$ as a ratio of the coefficient in front of $\delta f$ and the coefficient in front of $\delta\dot{f} = \delta f/\tau_c$ :

$$\tau_c^{-1} = \frac{K_{\mathrm{eff}} + \eta_{\mathrm{out}}V}{\eta_{\mathrm{eff}}R}. \qquad (2)$$

This provides us with $\tau_c$, the typical timescale of deformation of a RBC. We shall see from the numerical simulations

presented below that $\tau_c^{-1}$ is to a good approximation a linear function of $V$. Furthermore, we shall see that numerical simulation shows that the timescale is proportional to a linear combination of internal and external viscosities. Therefore, the above phenomenological law seems to constitute a quite reliable description when confronted with experimental and simulation results.

Let us rewrite Eq. 2 as

$$\tau_c^{-1} = a_1 V + a_0, \tag{3}$$

where

$$a_1^{-1} = R\alpha(1 + \beta\lambda + \gamma\lambda'), \tag{4}$$

$$a_0^{-1} = \frac{R\eta_{\text{out}}\alpha(1 + \beta\lambda + \gamma\lambda')}{K_{\text{eff}}}, \tag{5}$$

with

$$\lambda = \eta_{\text{in}}/\eta_{\text{out}},$$

$$\lambda' = \eta_{\text{mem}}/\eta_{\text{out}},$$

and where

$$\beta = \beta'/\alpha \text{ and } \gamma = \gamma'/\alpha.$$

The different coefficients above ($\alpha$, $\beta$, $\gamma$) can only be determined numerically (see below). However, when the shape of a cell is not very far from a sphere, an analytical calculation is possible (36–41). This has been done for the case of vesicles in a linear shear flow (39), taking into account $\eta_{\text{out}}$, $\eta_{\text{in}}$, and $\eta_{\text{mem}}$, and yields $\alpha \simeq 16/3$, $\beta \simeq 23/32$, and $\gamma = 1/2$. A similar study has been performed for a Poiseuille flow (41), incorporating only the contributions of the outer and inner fluid viscosities, which provides $\alpha \simeq 9$ and $\beta \simeq 76/85$ for the flow of a vesicle in a channel of internal radius 5 $\mu$m, as it is the case in our experiments. We discuss in Numerical and Analytical Results our choice for these parameters.

### *Numerical simulations*

We have performed a systematic numerical study of a model of RBC. The imposed flow is given by

$$\boldsymbol{V}^{\infty}(\boldsymbol{R}) = \boldsymbol{e}_x V\left[1 - \frac{y^2 + z^2}{(D/2)^2}\right], \tag{6}$$

where $V$ is the velocity at the center of the flow, the $x$ axis is along the flow direction, while the $y$ and $z$ axes are along the transverse directions. We consider here an unbounded flow. The sole role of the imposed Poiseuille flow curvature has proven to account for several experimental facts provided that the RBC is not too confined, as shown in Coupier et al. (42). $D/2$ in Eq. 6 is the distance from the center at which the velocity is zero, and was set equal to 5 $\mu$m as in the experiments described below.

Numerical simulations for three-dimensional models of RBCs are based on the boundary integral method, as originally described for vesicles in Biben et al. (43). Due to linearity of the Stokes equations, the total velocity of the RBC is the sum of the imposed flow (that is, parabolic and unbounded) and the one induced by the presence of RBC. Owing to the integral representation (boundary integral method), the dynamics of a RBC is represented by an integral on the RBC boundary and thus the external fluid domain can be taken as infinite. Recently (44), we have extended our initial work to include membrane shear elasticity mimicking the spectrin network of RBCs (membrane viscosity is not accounted for at present). We have also made several new numerical improvements that allowed us to study very deflated shapes, as required for simulation of real RBCs. We only provide here the main results concerning numerical determination of shapes and relaxation timescales, while details of the numerical techniques can be found in Farutin et al. (44). The RBC model takes into account both bending and shear elasticity. The Helfrich model is adopted for the bending energy, while the shear elasticity of the cytoskeleton is described using a strain-hardening model based on finite extensibility nonlinear elasticity, which has been able to capture some realistic features of RBCs (for details, see Farutin et al. (44)).

The RBC was modeled as an inextensible membrane, endowed with a shear modulus $\mu_s = 1.9\ \mu\text{N}\cdot\text{m}^{-1}$ and a bending modulus $\kappa = 2.7 \times 10^{-19}$ J. The stress-free state of the membrane was chosen as a biconcave shape with a surface area of 122 $\mu\text{m}^2$ and a volume of 82 $\mu\text{m}^3$ (i.e., $R \simeq 3$ $\mu$m). Most simulations were performed using 5120 triangular elements to discretize the membrane (2562 vertices). The viscosity of the inner solution of the cell was chosen as $\eta_{\text{in}} = 6$ mPa•s (8). The viscosity of the suspending medium, $\eta_{\text{out}}$, and the flow rate were varied as in the experiments. The elastic and geometrical parameters of the cell were chosen to get a model consistent with optical tweezers experiments (45). Several additional simulations were performed with different values of $\mu_s$ and $\kappa$ to mimic the chemical treatment of the cell.

The characteristic time of the cell was determined by monitoring the transient behavior of the cell velocity upon flow startup: in a manner similar to what has been used for experimental data analysis, we define the characteristic time $\tau_c$ as the time needed for the cell to reach 99% of its steady-state velocity.

## MATERIALS AND METHODS

### Materials

Fused silica capillaries of inner diameter 10 $\mu$m and outer diameter 150 $\mu$m were purchased from BGB Analytik (Rheinfelden, Germany). PDMS

(polydimethylsiloxane, Sylgard 184; Dow Corning, Midland, MI) was obtained from Neyco (Paris, France). BSA (bovine serum albumin), PBS (phosphate-buffered saline) tablets, dextran of average molecular mass 40 kDa, and diamide were purchased from Sigma-Aldrich (Lyon, France). Solutions of PBS 0.01 M and pH 7.4 were prepared using 18.2 MΩ•cm ultrapure water.

The viscosity of PBS and PBS + dextran solutions was measured on a cone/plate rheometer (MCR301; Anton Paar, Courtaboeuf, France), and found to be $\eta_{out} = 1.5 \pm 0.15$ mPa•s and $5 \pm 0.5$ mPa•s, respectively, for pure PBS and PBS + 10% weight of dextran 40 kDa. We have checked that both solutions behave as Newtonian fluids over the range of shear rates explored in this study.

## Preparation of blood samples

Blood samples from healthy donors were obtained through the Établissement Français du Sang (Grenoble, France) and stored at 4°C until use. Red blood cells were extracted from whole blood by successive washes in PBS solution and centrifugation. After each centrifugation, the supernatant was pipetted out and PBS was added to refill the tube. The washing/centrifugation cycle was repeated three times. RBCs were used as such, or after being exposed to diamide: using a protocol akin to that described in Forsyth et al. (22), erythrocytes were incubated at room temperature for 30 min in a PBS solution containing 5 mM of diamide, then washed in PBS before use in the flow cell.

## Experimental setup

Experiments were performed using a custom-built flow cell composed of the following elements, as illustrated in Fig. 1: four silica capillaries were cut in 3–6-mm-long segments and fitted into four grooves in the central band of a PDMS spacer. The spacer was then sandwiched between a glass coverslip and a clear polycarbonate plate, and the stack was clamped in an aluminum frame to ensure tight sealing of the cell. The inlet and outlet drilled into the polycarbonate upper plate were connected by silicone tubing to external reservoirs. A solenoid valve was connected between the inlet reservoir and the flow cell, to control the startup of the flow, while the steady-state flow velocity was controlled by adjusting the height difference ($\Delta z$) between the liquid-free surfaces in the inlet and outlet beakers. The response time upon startup of the whole setup (including valve, tubings, and flow cell) was measured to be $\lesssim$10 ms (see Fig. 4 *a* below).

Before the experiments, the flow cell was filled with a PBS solution containing 0.2% weight BSA, to coat the inner walls of the capillaries and prevent spurious adhesion of the cells to the walls of the microchannels. A RBC suspension was then added to the inlet reservoir and the concentration adjusted with PBS so that the initial bulk hematocrit was <1%.

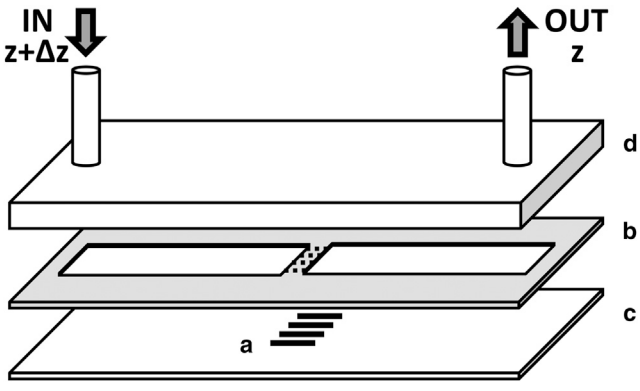


FIGURE 1 Sketch of the flow cell used in the startup experiments: (*a*) silica capillaries, (*b*) PDMS spacer with grooves, (*c*) glass coverslip, and (*d*) polycarbonate plate.

The flow cell was placed on the motorized stage of an inverted microscope (IX-71; Olympus, Melville, NY) equipped with a 100× oil-immersion objective. Image sequences of the flowing RBCs were acquired using a high-speed camera (Phantom Miro4, with chip size of 800 × 600 pixels; Vision Research, Ametek, Élancourt, France) at a frame rate of 4000 images/s. The imaging setup has a nominal sampling resolution of 0.21 $\mu$m/pixel and $2.5 \times 10^{-4}$ s.

## Experimental data analysis

The recorded image sequences were analyzed using toolboxes for IMAGEJ software (National Institutes of Health, Bethesda, MD) and MATLAB (The MathWorks, Natick, MA). Image stacks showing the position of a RBC inside the capillary as a function of time were opened with IMAGEJ and cropped to keep only a rectangular region of interest, of height 10 $\mu$m and length 167 $\mu$m, enclosing the lumen of the capillary focused at its midplane (see Fig. 2, *a–c*). The intensity of each image in the stack was averaged over the height of the region of interest, and the result of this averaging was plotted as a function of time, to obtain a space-time diagram (see Fig. 2 *d*). Such a space-time plot was further processed with a gradient filter and finally thresholded, to obtain a binary image showing the position of the front and rear parts of the flowing red blood cell as a function of time. This binary image was then processed with standard MATLAB software tools to extract the position of the front or rear ends as a function of time, $x(t)$, from which the instantaneous velocity $V_{RBC}(t)$ was computed. The accuracy in determining the position of the front/rear ends is on the order of the spatial extension of the RBC boundary on the images, namely 1 $\mu$m. To reduce the noise introduced when taking the time derivative of $x(t)$ to compute the velocity, we average the position data over a sliding time window of 5–15 points, yielding an actual time resolution of 1.25–3.75 ms. In practice, the accuracy of our velocity measurements is limited by such a noise, and is $\sim\pm$0.06–0.2 mm•s$^{-1}$, depending on the averaging. We have checked that no significant difference was obtained on $V_{RBC}(t)$ when computed from the position of the front or rear end, and that the obtained results were quantitatively in agreement with velocity measurements performed using particle-imaging-velocimetry tools from the software IMAGEJ. The method described above has the benefit of being much less time-consuming than particle-imaging velocimetry.

The characteristic transient time ($\tau_c$) of RBCs upon flow startup was determined in two different ways.

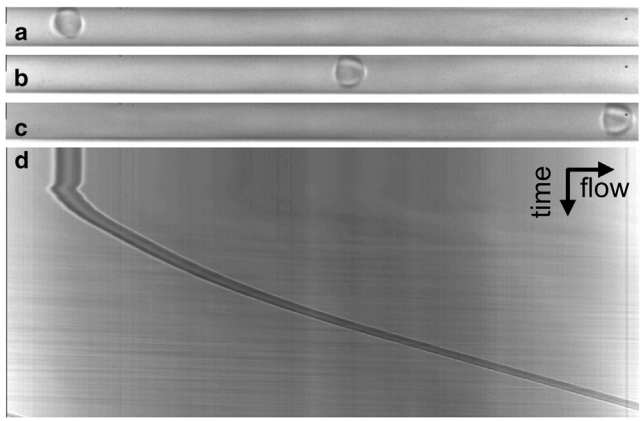


FIGURE 2 Image of a RBC in a channel at rest (*a*), during transient (*b*), and at steady state (*c*). (*d*) Space-time diagram built from the full image sequence: the diagram shows the averaged intensity along the flow direction (*horizontally*, flow is from *left* to *right*), as a function of time (*vertically*, from *top* to *bottom*). Image size is 167 $\mu$m × 85 ms. The steady-state velocity is 3 mm•s$^{-1}$, for a pressure drop of 2 kPa.

1. We have estimated $\tau_c$ from visual inspection of the time-dependent shape of RBCs, defining $\tau_c$ as the time above which no change in RBC shape was visible by eye; and
2. We have computed the transient time from RBC velocity, defining $\tau_c$ as the time required for a RBC to reach 90% of its steady-state velocity, as illustrated in Fig. 4 *a* below.

## RESULTS

### Measurements of transient time

An example of cell behavior during flow startup is given in Fig. 3 *a*. It can be seen that a RBC initially at rest in the channel gradually deforms with time, reaching a steady-state shape after a few tens of milliseconds. In the range of pressure drops explored in our work, the steady-state shape of the deformed RBC could be either parachute- or slipperlike (46–48), as illustrated in Fig. 3, *b–d*.

The time dependence of the velocity of a RBC ($V_{RBC}$) is illustrated in Fig. 4 *a*. From such $V_{RBC}(t)$ curves, we compute the following.

1. The steady-state velocity of the cells ($V_{max}$), which depends, as expected for a Poiseuille flow, linearly on the imposed pressure drop $\Delta P$, as shown in the inset of Fig. 4 *a*, and
2. The transient time $\tau_c$ as defined in Fig. 4 *a*.

In Fig. 4 *b*, we compare the characteristic time $\tau_c$ determined visually (from shape evolution) and from velocity transients, for all the data collected on RBCs suspended in PBS solution (the set of data corresponds to a total of ~100 cells). We find a good correlation between the times determined from the two methods, with $\tau_c$ computed from velocity being typically 20% smaller. This difference arises, to a large extent, from the criterion we use to define $\tau_c$ from velocity transients, which underestimates the time to actually reach steady state by 10–20%.

The results presented in the rest of the article correspond to $\tau_c$ determined from velocity transients. Data are presented as average values for $\tau_c$ and $V_{max}$, with error bars corresponding to $\pm 1$ SD, computed on groups of 8–12 RBCs.

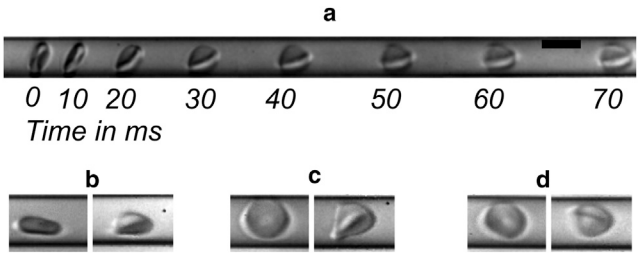


FIGURE 3 (*a*) Montage showing the time evolution of the shape of a RBC upon flow startup. Scale bar is 10 $\mu$m. Time is stamped below each image. The steady-state velocity reached by the RBC is $V_{max} = 2.8$ mm·s$^{-1}$. (*b–d*) Illustration of the variety of initial RBC configurations (*left image*) and final steady-state shapes (*right image*) observed in our experiments. The three RBCs shown on (*b*)–(*d*) reach the same $V_{max} = 0.88$ mm·s$^{-1}$.

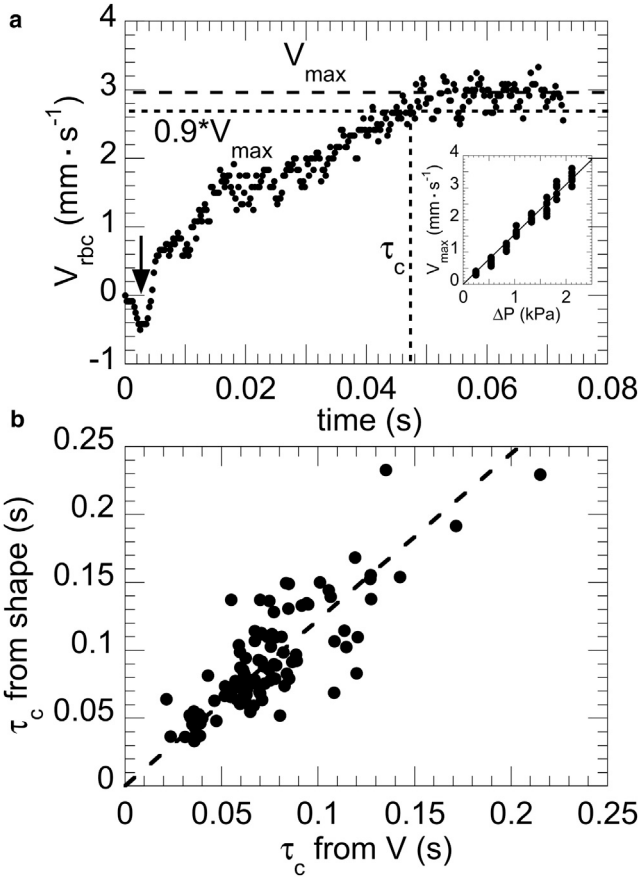


FIGURE 4 (*a*) (*Main panel*) Time evolution of the velocity of a RBC going from rest at $t = 0$ to a steady-state velocity $V_{max} = 3$ mm·s$^{-1}$. (*Arrow*) Typical velocity undershoot observed upon opening of the solenoid valve, which lasts <10 ms. (*Inset*) Dependence of $V_{max}$ on the imposed $\Delta P$. (*b*) The value $\tau_c$ determined from shape evolution as a function of $\tau_c$ computed from velocity transient. (*Dashed line*) Linear ($y = ax$) fit to the data, with slope $a = 1.22$.

Variability between individual RBCs probed under the same nominal conditions is the main source for the scattering observed on the measured transient times.

As can be seen in Fig. 3, a reason for such a scattering lies in the fact that the initial position and orientation of a RBC before flow startup could be highly variable from one cell to the next. Therefore, for a given flow condition, a velocity transient most likely reflects the combination of linear and angular transient deformations of a RBC, as well as centering of the cell in the channel if its starting position was off-axis. Distinguishing between angular and linear deformations would require three-dimensional or multiangle imagings of the RBCs (49), which are challenging experiments to perform at high rates and are beyond the scope of this study. On the other hand, we have checked that RBC centering did not affect greatly the value of $\tau_c$. To do so, we have complemented our measurements, in which gravity is oriented perpendicularly to the observation plane, by a set of experiments in which RBCs were observed in a

plane containing gravity. In the latter case, the initial position of RBCs was systematically biased toward the lower part of the capillary. As illustrated in Fig. 5 *a*, this did not result in any significant difference on $\tau_c$. Overall, the time $\tau_c$ determined using the above criterion is to be taken as an average characteristic time over the different deformation modes of a RBC upon flow startup. (The shape of the $V(t)$ curves, such as illustrated in Fig. 4 *a*, indeed shows that the approach to the steady state is not exponential. This suggests that velocity transients probably result from more than one single process.) Nevertheless, as we shall see in the discussion below, the excellent quantitative agreement between our results and those obtained from similar experiments based on advanced shape analysis of RBC transients (15) indicates that our scheme for the determination of $\tau_c$ provides meaningful information regarding the governing timescale.

## Dependence of $\tau_c$ on flow strength, external viscosity, and diamide treatment

We observe that the characteristic time $\tau_c$ decreases as the flow strength increases. This is illustrated in Fig. 5 *a*, for RBCs suspended in PBS solution, where it is seen that $\tau_c$ decreases from ~0.1 to 0.03 s as $V_{max}$ increases from 0.5 to 5 mm•s$^{-1}$.

Plotting the inverse time $1/\tau_c$ as a function of $V_{max}$, we find that $1/\tau_c$ exhibits a linear increase with the steady-state velocity (Fig. 5 *b*).

Upon increasing the viscosity of the suspending medium from that of PBS solution ($\eta_{out} = 1.5$ mPa•s) to that of the 10% weight dextran solution ($\eta_{out} = 5$ mPa•s), we observe that the dependence of $1/\tau_c$ on $V_{max}$ remains linear, with a greater slope than for RBCs suspended in PBS and a similar value of the intercept at zero velocity (Fig. 5 *b*).

Finally, we show in Fig. 6 the effect of diamide on transient time. It is seen that diamide-treated RBCs still exhibit an inverse transient time $1/\tau_c$ that increases linearly with $V_{max}$, with an overall upward shift of the curve with respect to that obtained for healthy RBCs.

As discussed in detail below, all the above results are in good agreement with the simple heuristic argument given in the Qualitative Discussion.

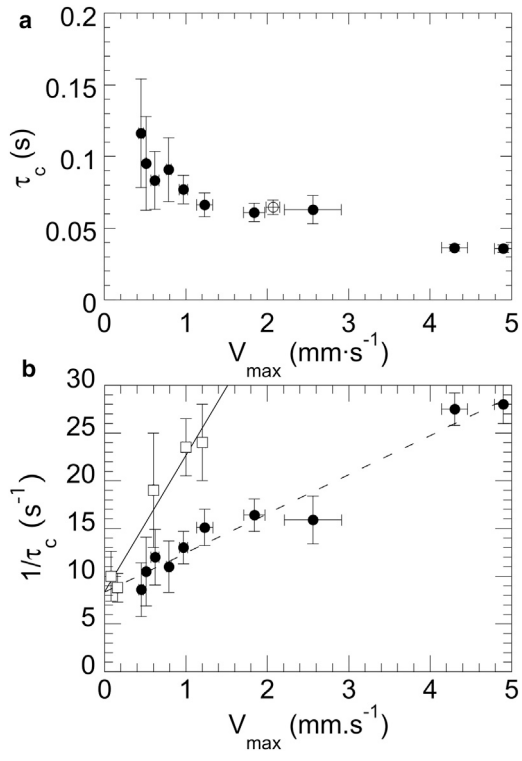


FIGURE 5 Dependence of $\tau_c$ on experimental parameters. (*a*) The value of $\tau_c$ as a function of $V_{max}$ for healthy RBCs suspended in PBS. (○) Determination of $\tau_c$ in conditions where the gravity biases the starting position of the RBCs, to evaluate the effect of the centering mechanism on the measured time. (*b*) $1/\tau_c$ as a function of $V_{max}$ for RBC in PBS (●) and in PBS containing 10% weight of dextran 40 kDa (□). (*Dashed line*) Linear fit, $\tau_c^{-1} = a_0 + a_1 V_{max}$, to the data obtained in PBS, with $a_0 = 8.3 \pm 0.8$ s$^{-1}$ and $a_1 = 4.1 \pm 0.3$ mm$^{-1}$. (*Solid line*) Linear fit to the data obtained in PBS + dextran, with $a_0 = 8.4 \pm 1.4$ s$^{-1}$ and $a_1 = 14.0 \pm 1.9$ mm$^{-1}$.

## Numerical results

Fig. 7 shows a snapshot illustrating the temporal evolution of the shape of a RBC obtained from simulations, starting from a biconcave shape at rest.

The inverse relaxation time is plotted in Fig. 8 as a function of the steady-state velocity. $1/\tau_c$ is seen to vary linearly with the flow rate, and to display a stronger dependence on $V_{max}$ for lower viscosity contrasts $\lambda$, i.e., for larger $\eta_{out}$ (see Fig. 8 *a*). There is no apparent deviation from linearity either for weak or for strong flows in the range of explored velocities, in qualitative agreement with experiments.

As shown in Fig. 8 *b*, for a given viscosity contrast $\lambda$, changing the value of the inner fluid viscosity, $\eta_{in}$, merely results in a vertical shift of the $\tau_c^{-1}(V_{max})$ curve, without

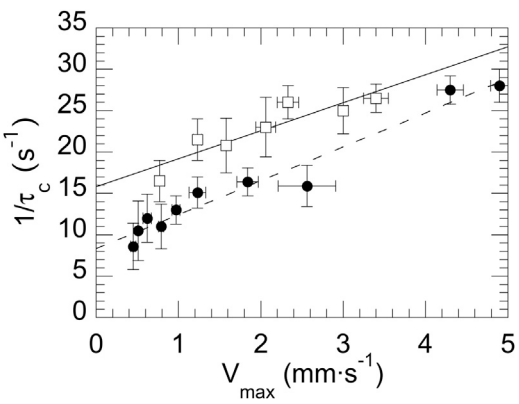


FIGURE 6 $1/\tau_c$ as a function of $V_{max}$ for untreated RBCs suspended in PBS (●), and diamide-treated RBCs in PBS (□). (*Lines*) Best linear fits of the data for untreated (*dashed line*, with slope and intercept values as in Fig. 5), and diamide-treated RBCs (*solid line*, $a_0 = 15.8 \pm 1.6$ s$^{-1}$ and $a_1 = 3.4 \pm 0.7$ mm$^{-1}$).

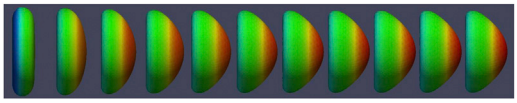

FIGURE 7 Numerical results illustrating the shape transformation for a RBC in Poiseuille flow. Color by surface tension. $V = 0.5$ mm•s$^{-1}$, $\lambda = 5$. To see this figure in color, go online.

affecting the slope. Data corresponding to an inner viscosity $\eta_{in}{}^{2}$ can be obtained from results computed for $\eta_{in}{}^{1}$ by simply rescaling $\tau_c{}^{-1}$ and $V_{max}$ by the ratio $\eta_{in}{}^{1}/\eta_{in}{}^{2}$.

The effect of varying the shear or the bending modulus is illustrated in Fig. 8 *b*. Decreasing $\mu_s$ by a factor of two leaves the slope of the curve essentially unchanged, and results in a twofold decrease of the intercept at zero velocity. Decreasing $\kappa$ by a factor of two increases the slope by 10% and lowers the offset at zero velocity by ~15%.

## DISCUSSION

### Numerical and analytical results

Fig. 7 illustrates the ability of the numerical model to reproduce the shape evolution of a RBC upon startup of a Poiseuille flow: the shape transition from discocyte to parachute obtained numerically is consistent with experimental observations such as that shown in Fig. 3 *a*.

There is a strikingly good qualitative agreement between the simulations and the model presented in Theoretical Framework. As inferred from a heuristic argument (Eq. 2), a linear dependence of $1/\tau_c$ on $V_{max}$ is predicted numerically; the slope of this linear dependence is controlled by the effective viscosity, hence by the ratio $\lambda$, while the elastic moduli affect only the value of $\tau_c{}^{-1}$ at $V_{max} = 0$. The magnitude of the effects produced by varying either $\mu_s$ or $\kappa$ indicates that the elastic behavior is essentially governed by $\mu_s$ (Fig. 8 *b*). In further support to our heuristic argument, we also find that the average membrane tension computed from numerical results is linearly dependent on flow velocity (Fig. 9 *a*), with a slope of ~1 mPa•s that is consistent with the value of $\eta_{out} = 1.5$ mPa•s. This confirms that, as mentioned in the Theoretical Framework section, membrane tension $\zeta$ is on the order of the external flow forcing $\eta_{out}V$.

Such an agreement between numerics and theory prompts us to further exploit numerical simulations. Fig. 8 *a* shows that the slope of $1/\tau_c$ versus $V_{max}$, called $a_1$ in Eq. 3, depends on the viscosity contrast $\lambda = \eta_{in}/\eta_{out}$. In Fig. 9, we plot the inverse slope, $a_1{}^{-1}$, obtained from numerical simulations, as a function of $\lambda$. It is seen that $a_1{}^{-1}$ increases linearly with $\lambda$.

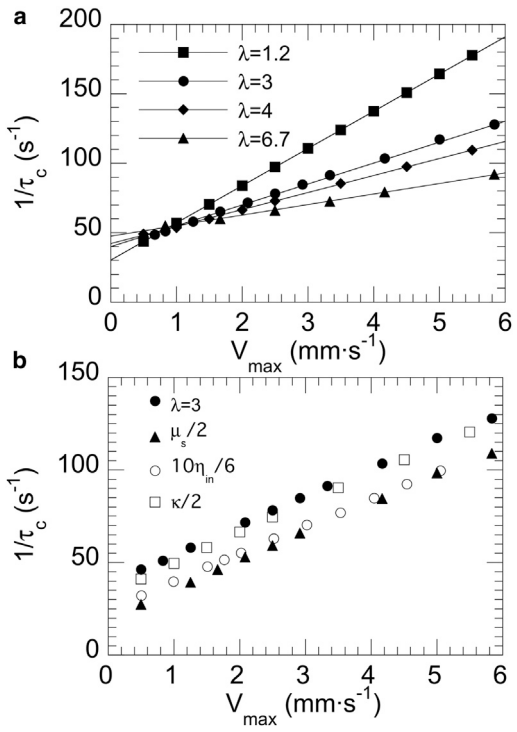


FIGURE 8 (*a*) Inverse relaxation time ($\tau_c{}^{-1}$) as a function of steady-state velocity ($V_{max}$), computed with $\eta_{in} = 6$ mPa•s, $\mu_s = 1.9$ $\mu$N•m$^{-1}$, and $\kappa = 2.7 \times 10^{-19}$ J, for various viscosity contrasts: (■) $\lambda = 1.2$, (●), $\lambda = 3$, (◆), $\lambda = 4$, and (▲) $\lambda = 6.7$. (*Solid lines*) Best linear fits to the data ($\tau_c{}^{-1} = a_0{}^{num} + a_1{}^{num}V_{max}$). (*b*) $\tau_c{}^{-1}$ ($V_{max}$) computed for $\lambda = 3$ and parameters as in (*a*) (●), with $\eta_{in} = 10$ mPa•s (○), with $\kappa = 1.35 \times 10^{-19}$ J (□); with $\mu_s = 0.95$ $\mu$N•m$^{-1}$ (▲).

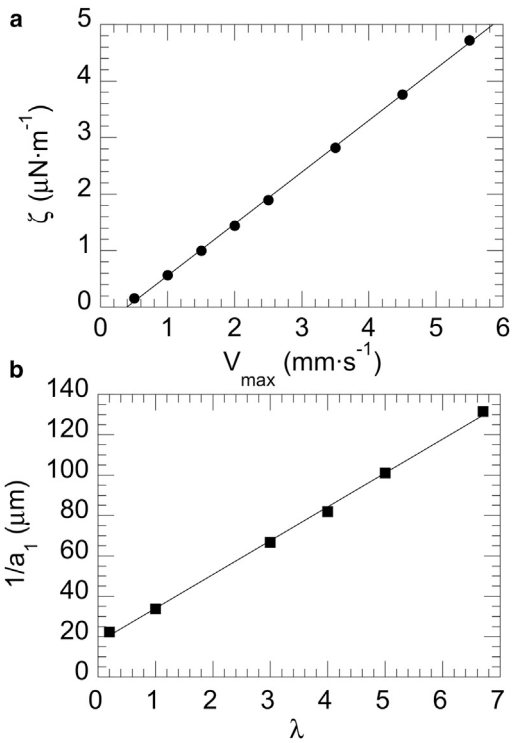


FIGURE 9 (*a*) Average membrane tension, $\zeta$, as a function of the maximum flow velocity $V_{max}$. Data obtained with a viscosity contrast $\lambda = 4$. (*Line*) Linear fit to the numerical data. (*b*) Inverse slope, $1/a_1$, as a function of viscosity contrast $\lambda$ (■). (*Solid line*) Best linear fit to the data, with a value of the intercept at $\lambda = 0$ of 17.2 $\mu$m and a slope of 16.8 $\mu$m.

This is again fully consistent with theoretical predictions (see Eq. 4). A linear fit of $a_1^{-1}(\lambda)$, therefore, allows us to determine the parameters $\alpha$ and $\beta$, which set the relative contributions of $\eta_{out}$ and $\eta_{in}$ to the effective viscosity (see Eq. 4): we get $\alpha R = 17.2$ $\mu$m and $\alpha R\beta = 16.8$ $\mu$m, which yields, with $R = 3$ $\mu$m, $\alpha = 5.7$, and $\beta = 0.98$. These values are to be compared with those predicted by theories, namely $\alpha \simeq 5.3$ and $\beta \simeq 0.72$ for the case of a linear shear flow (39), and $\alpha \simeq 9$ and $\beta \simeq 0.9$ for vesicles in a Poiseuille flow (41). The fair agreement between the parameters determined numerically and their theoretical values is satisfactory, all the more so that the analytical treatments proposed in Lebedev et al. (39) and Danker et al. (41) are based on spherical harmonics expansions that are strictly valid only for small deformations around a reference spherical shape, whereas numerical simulations handle the case of an initially biconcave, highly deflated, cell undergoing large deformations under flow. This provides strong support to the fact that analytical models such as those developed in Lebedev et al. (39) and Danker et al. (41) are robust and able to capture the main contributions to dissipation during vesicle flow.

On this basis, we will now analyze our experimental data within the proposed theoretical framework. Because numerical simulations account for more realistic shapes and deformations of the cells than theoretical models, we will use in the following the values of the parameters $\alpha$ and $\beta$ determined from the numerical results. As far as the parameter $\gamma$ is concerned, it cannot be determined from simulations because membrane viscosity is not included in the numerical model. Still, the reasonable agreement between the numerical and theoretical values obtained for $\alpha$ and $\beta$ suggests that analytical parameters are of the correct order of magnitude, and we will therefore use the theoretical value $\gamma = 1/2$ (39). A more accurate estimate of $\gamma$, i.e., of the exact weight of $\eta_{mem}$ in $\eta_{eff}$, would call for more advanced simulations accounting for membrane viscosity.

## Interpretation of experimental results for healthy RBC

We first compare our results with those obtained by Tomaiuolo and Guido (15): most of the results presented in their study have been obtained at a single steady-state velocity of 1 mm$\cdot$s$^{-1}$, at which $\tau_c = 0.09$ s is found for healthy RBCs in PBS. At the same velocity, we measure a characteristic time $\tau_c = 0.08 \pm 0.01$ s, which is in excellent quantitative agreement.

Besides, as predicted from a simple heuristic argument (see Eqs. 2 and 3), we find experimentally that $1/\tau_c$ is linear with $V_{max}$ (Fig. 5). Linear fits of the data obtained in PBS and PBS + dextran yield the values of the intercept at origin ($a_0$) and slope ($a_1$) reported in Table 1. We observe roughly a threefold increase in the slope when $\eta_{out}$ is multiplied by 3. Recalling that $a_1 = \eta_{out}/(\eta_{eff}R)$ (Eq. 2), this suggests that $\eta_{eff}$ is only marginally affected by the external viscosity for $\eta_{out}$ in the range 1.5–5 mPa$\cdot$s, hence that the contribution of $\eta_{out}$ to $\eta_{eff}$ is weak. This is also consistent with the fact that the change in $\eta_{out}$ does not modify significantly the value of $a_0 = K_{eff}/(\eta_{eff}R)$. In our experiments, the main effect of changing $\eta_{out}$ is therefore to affect the magnitude of the hydrodynamic forces ($\eta_{out}V$) applied to the RBC.

**TABLE 1 Values of $a_0$ and $a_1$ obtained from a linear fit of the experimental data for RBCs suspended in PBS ($\eta_{out} = 1.5$ mPa$\cdot$s) and in PBS + dextran ($\eta_{out} = 5$ mPa$\cdot$s)**

| $\eta_{out}$ (mPa$\cdot$s) | $a_0$ (s$^{-1}$) | $a_1$ (mm$^{-1}$) | $\eta_{eff}$ (mPa$\cdot$s) | $K_{eff}$ ($\mu$N$\cdot$m$^{-1}$) | $\eta_{mem}$ (mPa$\cdot$s) |
|---|---|---|---|---|---|
| 1.5 | 8.3 ± 0.8 | 4.1 ± 0.3 | 122 ± 21 | 3.0 ± 0.8 | 28 ± 8 |
| 5 | 8.4 ± 1.4 | 14.0 ± 1.9 | 119 ± 28 | 3.0 ± 1.2 | 20 ± 11 |

The corresponding values of $\eta_{eff}$ and $K_{eff}$ have been computed from Eqs. 2 and 3 with $R = 3$ $\mu$m. The membrane viscosity $\eta_{mem}$ has been calculated from $\eta_{eff}$ using Eq. 4 with $R = 3$ $\mu$m, $\alpha = 5.7$, $\beta = 0.98$, $\gamma = 0.5$, and $\eta_{in} = 6$ mPa$\cdot$s.

From $a_0$ and $a_1$, we compute the effective viscosity and elastic modulus that are given in Table 1. We thus get a value of $\eta_{eff} \simeq 120$ mPa$\cdot$s, which is in good agreement with the one reported in a recent study by Betz et al. (8), namely $\eta_{eff} \simeq 100$ mPa$\cdot$s. The value of $K_{eff} \simeq 3$ $\mu$N$\cdot$m$^{-1}$ is consistent with that of 2.5 ± 0.4 $\mu$N$\cdot$m$^{-1}$ reported for $\mu_s$ by Hénon et al. (50). This suggests that, in the experimental conditions used in this study, $K_{eff}$ is governed by the shear elastic modulus. This is in agreement with our numerical results, which show that the value of $\tau_c^{-1}$ at $V_{max} = 0$ is essentially controlled by $\mu_s$ (Fig. 8 *b*).

Furthermore, from the values of $a_1$ and using Eq. 4, we make the following estimates for the membrane viscosity: $\eta_{mem} \simeq 20$–$28$ mPa$\cdot$s (see Table 1). From such an estimate, we conclude that, for an outer fluid viscosity in the physiological range ($\eta_{out} \sim 1$ mPa$\cdot$s), $\eta_{in}$ and $\eta_{mem}$ are the two major contributions to the effective viscosity: $\alpha(\beta\eta_{in} + \gamma\eta_{mem}) \simeq 100$ mPa$\cdot$s $\simeq \eta_{eff}$. Finally, if we compute a two-dimensional membrane viscosity as $\eta_{mem}^{2D} = \eta_{mem}R$, we get $\eta_{mem}^{2D} \simeq 0.6$–$0.85 \times 10^{-7}$ N$\cdot$s$\cdot$m$^{-1}$.

To summarize, our results regarding the order of magnitude of $\tau_c$ are consistent with those from previous works on the transient response of RBCs (15,16,26), but on the other hand we estimate a membrane viscosity $\eta_{mem}^{2D}$, which is approximately one order-of-magnitude lower than the values reported in these studies (i.e., $\eta_{mem}^{2D} \sim 10^{-6}$ N$\cdot$s$\cdot$m$^{-1}$ (26)). However, we note that the latter are based on an analysis proposed initially by Evans and Hochmuth (30), who developed a model assuming that the only dissipation relevant to RBC shape recovery is associated with the membrane viscosity. They thereby neglected dissipation in the inner and outer fluids, and estimated $\eta_{mem}^{2D} \simeq \tau_c\mu_s$. By contrast, here we make no such assumption. We find that 1) the effective viscosity is a combination of $\eta_{mem}$, $\eta_{in}$, and $\eta_{out}$; and 2) each viscosity entering $\eta_{eff}$ has a weight that is larger than 1 ($\alpha \simeq 6$). The latter point, which is an

output of our theoretical and numerical analysis, is consistent with the ad hoc assumption made by Betz et al. (8) in their modeling of membrane fluctuations. Taking into account all the viscous contributions and their respective weights in our data analysis, we get values for $\eta_{mem}^{2D}$ in very good agreement with those reported by Tran-Son-Tay et al. (32). These authors deduced $\eta_{mem}^{2D}$ from the tank-treading frequencies of RBCs under shear, using a model incorporating all dissipation sources, and obtained values that lie between 0.5 and 1.2 $\times$ $10^{-7}$ N•s•m$^{-1}$. Our work, fully consistent with the one of Tran-Son-Tay et al. (32), thus strongly suggests that the assumption made by Evans and Hochmuth (30) leads to an overestimate of $\eta_{mem}^{2D}$ and is at the origin of the apparent discrepancy between the reported values of RBC membrane viscosity.

## Comparison between experiments and numerical simulations

Although numerical simulations show a linear dependence of $1/\tau_c$ on $V_{max}$, in qualitative agreement with experiments, we observe that both the slope ($a_1^{num}$) and the extrapolated value of $1/\tau_c$ at zero velocity ($a_0^{num}$) predicted numerically are larger than the experimental values ($a_1^{exp}$ and $a_0^{exp}$). This is shown in the summary table below (Table 2).

Following the data analysis proposed in the previous section, the difference in slopes can straightforwardly be attributed to the contribution of membrane viscosity to the effective viscosity. Indeed, we have used the numerical results regarding $a_1^{num}(\lambda)$ to determine the parameters $\alpha$ and $\beta$ (Fig. 9), and then fitted the experimental data using Eqs. 3 and 4 to evaluate $\eta_{mem}$, so that the difference between the inverse slopes merely reads $1/a_1^{exp} - 1/a_1^{num} = \alpha\gamma R\eta_{mem}/\eta_{out}$. Using the latter expression to compute $\eta_{mem}$ yields exactly the same values reported before for the membrane viscosity.

Now, a much more stringent test is to check whether the difference in the offsets ($a_0$) can be attributed to the contribution of membrane viscosity, because in contrast to $a_1^{num}$, $a_0^{num}$ was not used to determine parameters of the model. From Eq. 5, we expect

$$\frac{1}{a_0^{exp}} - \frac{1}{a_0^{num}} = \frac{\alpha\gamma\eta_{mem}R}{K_{eff}}. \quad (7)$$

To check the above equality, we estimate $K_{eff}$ from Eq. 7 and compare it to the effective modulus determined in the previous section. Using the values of $a_0$ reported in Table 2 and of $\eta_{mem}$ determined above, we get $K_{eff}$ = 2–2.5 $\mu$N•m$^{-1}$, respectively, for $\lambda = 1.2$ ($\eta_{out} = 5$ mPa•s) and $\lambda = 4$ ($\eta_{out} =$ 1.5 mPa • s). This is in quantitative agreement with the value of $K_{eff} \simeq 3 \pm 1$ $\mu$N•m$^{-1}$ determined from experimental data, and therefore supports the fact that discrepancies between simulations and experiments are due to the missing contribution of membrane viscosity in the numerical model.

**TABLE 2 Comparison of numerical and experimental values of $a_0$ and $a_1$**

| $\lambda$ | $a_0^{num}$ (s$^{-1}$) | $a_1^{num}$ (mm$^{-1}$) | $a_0^{exp}$ (s$^{-1}$) | $a_1^{exp}$ (mm$^{-1}$) |
|---|---|---|---|---|
| 4 | 42.1 | 12.3 | 8.3 | 4.1 |
| 1.2 | 30.3 | 26.8 | 8.4 | 14.0 |

## Effect of diamide treatment

In Fig. 6, we see that treating RBCs with diamide mainly results in an upward shift of the curve $\tau_c^{-1}(V_{max})$, i.e., diamide-treated RBCs exhibit a shorter transient time than healthy ones. From a linear fit to the data, we obtain $\eta_{eff} =$ 147 $\pm$ 45 mPa•s and $K_{eff} = 7.0 \pm 2.8$ $\mu$N•m$^{-1}$. The major effect of diamide is therefore an increase of the effective elastic modulus $K_{eff}$, by roughly a factor of 2 with respect to healthy RBCs. Diamide is known to affect the spectrin network of RBCs, by creating cross links between proteins through the formation of disulphide bonds (51). Such a cross-linking process has been reported to induce a stiffening of RBCs (51–54), via an increase in the membrane shear modulus (51). Our results concerning the effect of diamide on RBC transient time are therefore fully consistent with these previous studies. Furthermore, attributing the increase of $K_{eff}$ to an increase in $\mu_s$ is consistent with the values presented in the Numerical Results. However, Forsyth et al. (22), from which we have adapted the protocol for diamide treatment in this work, recently reported that, in microfluidics experiments relying on cell stretching during transient confinement in a channel constriction, no difference in elongation could be detected between healthy and diamide-treated RBCs. We believe that the apparent contradiction between our finding and the conclusions of Forsyth et al. (22) merely arises from the very different timescales probed in the two studies. Indeed, while we characterize the effect of diamide by measuring the transient viscoelastic time of RBCs, on the order of 50 ms, Forsyth et al. probe the elongation of RBCs during a transient confinement that lasts between 1 and 5 ms only (calculated from the flow speeds and constriction length reported in Forsyth et al. (22)). The duration of confinement in the work of Forsyth et al. is therefore much shorter than the time required for RBCs to reach their steady shape. This, added to the fact that we have used both a slightly larger diamide concentration and treatment time in our study, is likely to be at the origin of the differences between our work and the one reported in Forsyth et al. (22).

## CONCLUSIONS

We have performed a study of the characteristic viscoelastic time $\tau_c$ of red blood cells. We have combined theory and numerical simulations to establish a framework for the analysis of flow startup experiments on RBCs confined into

microchannels. We have obtained experimental values of $\tau_c$ in quantitative agreement with those from previous studies, measured either from flow startup (15), relaxation after cessation of shear (27), or micropipette experiments (26). Moreover, we have shown that probing the dependence of $\tau_c$ on flow strength allows us to determine both the effective viscosity ($\eta_{\mathrm{eff}}$) and elastic modulus ($K_{\mathrm{eff}}$), and have obtained values for these two quantities which are consistent with those from other works (8,50). Most importantly, we have shown that, in contrast to the assumption made by Evans and Hochmuth (30) and commonly used later (15,16,26,27), $\eta_{\mathrm{eff}}$ is not equal to the membrane viscosity $\eta_{\mathrm{mem}}$. We have identified, from theory and simulations, the relative contributions of the membrane, inner ($\eta_{\mathrm{in}}$) and outer ($\eta_{\mathrm{out}}$) fluid viscosities to the overall effective viscosity, and used this to compute the value of the membrane viscosity from our experimental data. Doing so, we obtain $\eta_{\mathrm{mem}}$ in the range 20–28 mPa•s, which translates into a two-dimensional viscosity $\eta_{\mathrm{mem}}^{\mathrm{2D}} = 0.6\text{–}0.85 \times 10^{-7}$ N•s•m$^{-1}$. We conclude that the difference of up to one order of magnitude that can be found in the literature regarding $\eta_{\mathrm{mem}}$ only results from the fact that assuming $\eta_{\mathrm{eff}} \equiv \eta_{\mathrm{mem}}$ leads to overestimate $\eta_{\mathrm{mem}}$ by approximately a factor of 10. This work thus reconciles previous contrasting reports about RBC membrane viscosity, and provides a range of values for $\eta_{\mathrm{mem}}^{\mathrm{2D}}$ that is in excellent quantitative agreement with the result of Tran-Son-Tay et al. (32). Moreover, we have demonstrated that measuring $\tau_c$ as a function of flow strength provides valuable information not only on dissipation, but also on the elastic response of RBCs, and is sensitive to elasticity alterations such as those caused by diamide. This type of experimental investigation, analyzed within the proposed framework, should therefore prove to be useful in discriminating how physical or biological factors may affect red blood cell elasticity or viscosity.

## SUPPORTING MATERIAL

Supporting Material is available at http://www.biophysj.org/biophysj/supplemental/S0006-3495(15)00308-2.

## ACKNOWLEDGMENTS

We acknowledge financial support from the Centre National d'Etudes Spatiales, the European Space Agency, and the Université Franco-Allemande, Collège Doctoral "Liquides Vivants" (to A.F.).

## REFERENCES

1. Baskurt, O. K., and H. J. Meiselman. 2003. Blood rheology and hemodynamics. *Semin. Thromb. Hemost.* 29:435–450.
2. Fedosov, D. A., W. Pan, …, G. E. Karniadakis. 2011. Predicting human blood viscosity in silico. *Proc. Natl. Acad. Sci. USA.* 108:11772–11777.
3. Fedosov, D. A., H. Noguchi, and G. Gompper. 2014. Multiscale modeling of blood flow: from single cells to blood rheology. *Biomech. Model. Mechanobiol.* 13:239–258.
4. Ghigliotti, G., T. Biben, and C. Misbah. 2010. Rheology of a dilute two-dimensional suspension of vesicles. *J. Fluid Mech.* 653:489–518.
5. Chien, S. 1987. Red cell deformability and its relevance to blood flow. *Annu. Rev. Physiol.* 49:177–192.
6. Hochmuth, R. M., and R. E. Waugh. 1987. Erythrocyte membrane elasticity and viscosity. *Annu. Rev. Physiol.* 49:209–219.
7. Kim, Y., K. Kim, and Y. Park. 2012. Measurement techniques for red blood cell deformability: recent advances. *In* Blood Cell—An Overview of Studies in Hematology. T. E. Moschandreou, editor. Intech, Rijeka, Croatia, pp. 167–194.
8. Betz, T., M. Lenz, …, C. Sykes. 2009. ATP-dependent mechanics of red blood cells. *Proc. Natl. Acad. Sci. USA.* 106:15320–15325.
9. Fedosov, D. A., B. Caswell, and G. E. Karniadakis. 2010. A multiscale red blood cell model with accurate mechanics, rheology, and dynamics. *Biophys. J.* 98:2215–2225.
10. Li, J., G. Lykotrafitis, …, S. Suresh. 2007. Cytoskeletal dynamics of human erythrocyte. *Proc. Natl. Acad. Sci. USA.* 104:4937–4942.
11. Peng, Z., X. Li, …, S. Suresh. 2013. Lipid bilayer and cytoskeletal interactions in a red blood cell. *Proc. Natl. Acad. Sci. USA.* 110:13356–13361.
12. Dimitrakopoulos, P. 2012. Analysis of the variation in the determination of the shear modulus of the erythrocyte membrane: effects of the constitutive law and membrane modeling. *Phys. Rev. E Stat. Nonlin. Soft Matter Phys.* 85:041917.
13. Mohandas, N., and P. G. Gallagher. 2008. Red cell membrane: past, present, and future. *Blood.* 112:3939–3948.
14. Kwan, J. M., Q. Guo, …, M. D. Scott. 2013. Microfluidic analysis of cellular deformability of normal and oxidatively damaged red blood cells. *Am. J. Hematol.* 88:682–689.
15. Tomaiuolo, G., and S. Guido. 2011. Start-up shape dynamics of red blood cells in microcapillary flow. *Microvasc. Res.* 82:35–41.
16. Tomaiuolo, G., M. Barra, …, S. Guido. 2011. Microfluidics analysis of red blood cell membrane viscoelasticity. *Lab Chip.* 11:449–454.
17. Secomb, T. W., R. Skalak, …, J. F. Gross. 1986. Flow of axisymmetric red blood cells in narrow capillaries. *J. Fluid Mech.* 163:405–423.
18. Secomb, T. W., and R. Hsu. 1996. Analysis of red blood cell motion through cylindrical micropores: effects of cell properties. *Biophys. J.* 71:1095–1101.
19. Fedosov, D. A., M. Peltomäki, and G. Gompper. 2014. Deformation and dynamics of red blood cells in flow through cylindrical microchannels. *Soft Matter.* 10:4258–4267.
20. Kaoui, B., J. Harting, and C. Misbah. 2011. Two-dimensional vesicle dynamics under shear flow: effect of confinement. *Phys. Rev. E Stat. Nonlin. Soft Matter Phys.* 83:066319.
21. Thiébaud, M., Z. Shen, …, C. Misbah. 2014. Prediction of anomalous blood viscosity in confined shear flow. *Phys. Rev. Lett.* 112:238304.
22. Forsyth, A. M., J. Wan, …, H. A. Stone. 2010. The dynamic behavior of chemically "stiffened" red blood cells in microchannel flows. *Microvasc. Res.* 80:37–43.
23. Rosenbluth, M. J., W. A. Lam, and D. A. Fletcher. 2008. Analyzing cell mechanics in hematologic diseases with microfluidic biophysical flow cytometry. *Lab Chip.* 8:1062–1070.
24. Shevkoplyas, S. S., T. Yoshida, …, M. W. Bitensky. 2006. Direct measurement of the impact of impaired erythrocyte deformability on microvascular network perfusion in a microfluidic device. *Lab Chip.* 6:914–920.
25. Hou, H. W., A. A. S. Bhagat, …, C. T. Lim. 2010. Deformability based cell margination—a simple microfluidic design for malaria-infected erythrocyte separation. *Lab Chip.* 10:2605–2613.
26. Hochmuth, R. M., P. R. Worthy, and E. A. Evans. 1979. Red cell extensional recovery and the determination of membrane viscosity. *Biophys. J.* 26:101–114.
27. Baskurt, O. K., and H. J. Meiselman. 1996. Determination of red blood cell shape recovery time constant in a Couette system by the analysis of light reflectance and ektacytometry. *Biorheology.* 33:489–503.

28. Bronkhorst, P. J. H., G. J. Streekstra, …, G. J. Brakenhoff. 1995. A new method to study shape recovery of red blood cells using multiple optical trapping. *Biophys. J.* 69:1666–1673.

29. Braunmüller, S., L. Schmid, …, T. Franke. 2012. Hydrodynamic deformation reveals two coupled modes/time scales of red blood cell relaxation. *Soft Matter.* 8:11240–11248.

30. Evans, E. A., and R. M. Hochmuth. 1976. Membrane viscoelasticity. *Biophys. J.* 16:1–11.

31. Chien, S., K.-L. P. Sung, …, A. Tözeren. 1978. Theoretical and experimental studies on viscoelastic properties of erythrocyte membrane. *Biophys. J.* 24:463–487.

32. Tran-Son-Tay, R., S. P. Sutera, and P. R. Rao. 1984. Determination of red blood cell membrane viscosity from rheoscopic observations of tank-treading motion. *Biophys. J.* 46:65–72.

33. Riquelme, B. D., J. R. Valverde, and R. J. Rasia. 2000. Determination of the complex viscoelastic parameters of human red blood cells by laser diffractometry. *In* Optical Diagnostics of Biological Fluids, Vol. 3923. Proceedings of SPIE, San Jose, CA. 132–140.

34. Fischer, T. M. 2007. Tank-tread frequency of the red cell membrane: dependence on the viscosity of the suspending medium. *Biophys. J.* 93:2553–2561.

35. Secomb, T. W., B. Styp-Rekowska, and A. R. Pries. 2007. Two-dimensional simulation of red blood cell deformation and lateral migration in microvessels. *Ann. Biomed. Eng.* 35:755–765.

36. Misbah, C. 2006. Vacillating breathing and tumbling of vesicles under shear flow. *Phys. Rev. Lett.* 96:028104.

37. Danker, G., T. Biben, …, C. Misbah. 2007. Dynamics and rheology of a dilute suspension of vesicles: higher-order theory. *Phys. Rev. E Stat. Nonlin. Soft Matter Phys.* 76:041905.

38. Vlahovska, P. M., and R. S. Gracia. 2007. Dynamics of a viscous vesicle in linear flows. *Phys. Rev. E Stat. Nonlin. Soft Matter Phys.* 75:016313.

39. Lebedev, V. V., K. S. Turitsyn, and S. S. Vergeles. 2008. Nearly spherical vesicles in an external flow. *New J. Phys.* 10:043044.

40. Vlahovska, P. M., Y. N. Young, …, C. Misbah. 2011. Dynamics of a non-spherical microcapsule with incompressible interface in shear flow. *J. Fluid Mech.* 678:221–247.

41. Danker, G., P. M. Vlahovska, and C. Misbah. 2009. Vesicles in Poiseuille flow. *Phys. Rev. Lett.* 102:148102.

42. Coupier, G., A. Farutin, …, C. Misbah. 2012. Shape diagram of vesicles in Poiseuille flow. *Phys. Rev. Lett.* 108:178106.

43. Biben, T., A. Farutin, and C. Misbah. 2011. Three-dimensional vesicles under shear flow: numerical study of dynamics and phase diagram. *Phys. Rev. E Stat. Nonlin. Soft Matter Phys.* 83:031921.

44. Farutin, A., T. Biben, and C. Misbah. 2014. 3D numerical simulations of vesicle and inextensible capsule dynamics. *J. Comput. Phys.* 275:539.

45. Mills, J. P., L. Qie, …, S. Suresh. 2004. Nonlinear elastic and viscoelastic deformation of the human red blood cell with optical tweezers. *Mech. Chem. Biosys.* 1:169–180.

46. Skalak, R., and P. I. Branemark. 1969. Deformation of red blood cells in capillaries. *Science.* 164:717–719.

47. Secomb, T. W., and R. Skalak. 1982. A two-dimensional model for capillary flow of an asymmetric cell. *Microvasc. Res.* 24:194–203.

48. Kaoui, B., G. Biros, and C. Misbah. 2009. Why do red blood cells have asymmetric shapes even in a symmetric flow? *Phys. Rev. Lett.* 103:188101.

49. Dupire, J., M. Socol, and A. Viallat. 2012. Full dynamics of a red blood cell in shear flow. *Proc. Natl. Acad. Sci. USA.* 109:20808–20813.

50. Hénon, S., G. Lenormand, …, F. Gallet. 1999. A new determination of the shear modulus of the human erythrocyte membrane using optical tweezers. *Biophys. J.* 76:1145–1151.

51. Fischer, T. M., C. W. M. Haest, …, B. Deuticke. 1978. Selective alteration of erythrocyte deformability by SH-reagents: evidence for an involvement of spectrin in membrane shear elasticity. *Biochim. Biophys. Acta.* 510:270–282.

52. Johnson, G. J., D. W. Allen, …, J. G. White. 1980. Decreased survival in vivo of diamide-incubated dog erythrocytes. A model of oxidant-induced hemolysis. *J. Clin. Invest.* 66:955–961.

53. Rodrigues, R. O., V. Faustino, …, R. Lima. 2013. Red blood cells deformability index assessment in a hyperbolic microchannel: the diamide and glutaraldehyde effect. *WebmedCentral. Biomed. Eng. (N.Y.).* 4:WMC004375.

54. Shin, S., Y. Ku, …, J. Suh. 2005. Disposable biosensor for measuring red blood cell deformability using laser-diffraction technique. *In* Biomedical Applications of Micro- and Nanoengineering II, Vol. 5651. Proceedings of SPIE, Bellingham, WA. 68–77.